Structural stability of Polylactide rope drums with a hybrid Gyroid-spokes infill structure, manufactured through fused filament fabrication

Dipl.-Ing. Raimond Hofmann[1*], Armin Bochert[1], Prof. Dr.-Ing. habil. Thorsten Schmidt[1]

[1] Institute of Material Handling and Industrial Engineering, Faculty of Mechanical Science and Engineering, Technische Universität Dresden

* Correspondence: raimond.hofmann@tu-dresden.de; Tel.: +49-351-463-36744

ABSTRACT Additive manufacturing (AM) offers greater design freedom than conventional manufacturing processes. AM allows for components with complex infill structures of e. g. triply periodic-minimal surfaces (TPMS) that lead to significant weight reduction. Nevertheless, AM is mainly used in specialised engineering branches such as aerospace and medical engineering. This is due to high system cost and the high energy costs of the machines used, which utilise selective laser sintering (SLS), laser powder bed fusion (LPBF), or stereolithography (SLA). Fused filament fabrication (FFF) can offer cheaper and more energy-efficient machines. A series of tensile tests with FFF rope drum bodies made from polylactide (PLA) aims to investigate the stability of FFF machine elements. The test specimens possess a novel, hybrid infill structure comprised of straight spokes and a TPMS-gyroid surface. Compared to previous investigations, the specific breaking force – relative to the test specimens' weight – increased by up to 159%. Whereas the infill density affects tensile strength as well as deformation, the infill distribution between the TPMS and spokes part of said hybrid structure affects especially the deformation behaviour. The results show that FFF machine elements such as the tested drum bodies have a realistic perspective for use in future products with regard to static strength.

Symbol directory

B	Drum width in mm
D	Drum diameter in mm
D_N	Hub diameter in mm
F_b	Breaking force in kN
F^*_b	Specific breaking force in kN/kg
V_{res}	Total infill volume in cm³
V_{Sp}	Spokes infill volume in cm³
V_{TPMS}	Gyroid-TPMS infill volume in cm³
d_l	Nominal rope diameter in mm
h_R	Rope groove diameter in mm
l_C	Cell size in mm
m_T	Mass drum body in g
n	Layer count
n_C	Cell count
n_{Sp}	Spoke count
n_W	Winding count
p	Groove gradient in mm
r_l	Groove radius in mm
t	Offset between TPMS and isosurface
t_p	Print time in hh:mm
z	Stroke in mm
z_w	Drum length in mm
z_N	Teeth count
α_{St}	Angle in gradient area in °
μ	Infill distribution
ρ	Infill density
σ_V	Equivalent stress in N/mm²

1. Introduction

Additive manufacturing (AM) processes allow for complex designs that are not possible with conventional manufacturing processes. The combination of multi-part assemblies into complex individual parts reduces a product's number of parts and production steps. By designing components not solid, but with porous infill structures, a significant reduction in weight is possible.

Triply periodic minimal surfaces (TPMS) are often used for this purpose. These are isosurfaces defined by the roots of various implicit equations [1], whereby Schwarz P, D and G see wide application in AM. Schwarz G (also called gyroid) for example can be described as

$$G = \sin\left(\frac{2\pi}{a}x\right)\cos\left(\frac{2\pi}{b}y\right) + \sin\left(\frac{2\pi}{b}y\right)\cos\left(\frac{2\pi}{c}z\right) + \sin\left(\frac{2\pi}{c}z\right)\cos\left(\frac{2\pi}{a}x\right) = t. \qquad (1)$$

With this equation it is possible to create the basic shape of the so-called unit cell, which is the least common multiple of the desired infill structure. Through adjusting the coefficients a, b, and c, the shape of the unit cell transforms in all three spatial directions, which can be used for optimisation. The offset t shifts the entire TPMS within the unit cell's (usually cube-shaped) boundary volume. For t=0, a TPMS is created that divides the volume in two halves of equal size (**Figure 1**).

The complex design of TPMS offers various unique features but prevents the use of conventional manufacturing methods. TPMS can be used to generate volume or shell lattices. For volume lattices, the TPMS cuts the cube-shaped volume and one of the two halves ends up as the desired lattice (G_{t1}, G_{t2}). Shell lattices are created by using two partial volumes that result from different values for t (G_l). It is also possible to create volume and shell lattices with varying material thickness to adapt them to distinct load cases [2, 3]. Multiple mutually enclosing and non-contacting shell-lattices can be created and manufactured in one step, for example to combine different materials into a hybrid component using multi-material printing [4].
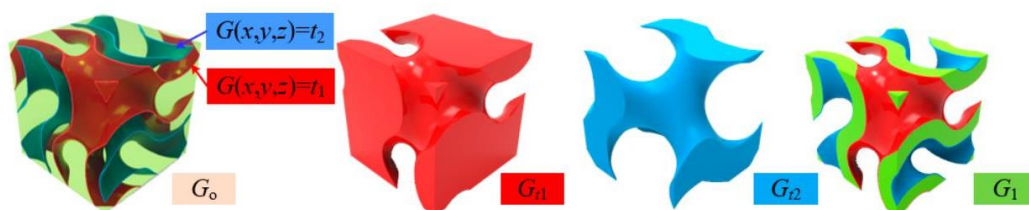

Figure 1: Modelling shell lattices [4].

Nowadays there is a wide range of AM processes. Processes such as selective laser sintering (SLS), laser powder bed fusion (LPBF), or stereolithography (SLA) make use of highly complex, expensive production machines and are primarily used in aerospace and medical engineering [3, 5]. As of now it is financially unattractive to produce conventional machine elements with such manufacturing machines.

An economically more attractive manufacturing process is therefore necessary to exploit the advantages of AM for classic machine elements; such as gear wheels, shafts, pulleys, rope pulleys, or rope drums. The fused filament fabrication (FFF) process, in which thermoplastic filaments are heated and subsequently extruded, is one such process. The necessary 3D printers are simpler in design, which translates into significantly lower acquisition costs. This results in a wide range of (consumer) FFF 3D printers. In addition, production with FFF is cheaper than with SLS, LPBF or SLA [6].

Aside from other thermoplastics, FFF also processes polylactide (PLA). PLA consists of 100% renewable resources (plant starch), is mechanically or chemically recyclable, and compostable under controlled conditions [7]. Sustainable cultivation of the needed raw materials could yield a negative CO_2 balance [8]. The use of PLA with FFF can lead to more sustainable machine elements; all the way to a nearly zero-waste product life cycle.
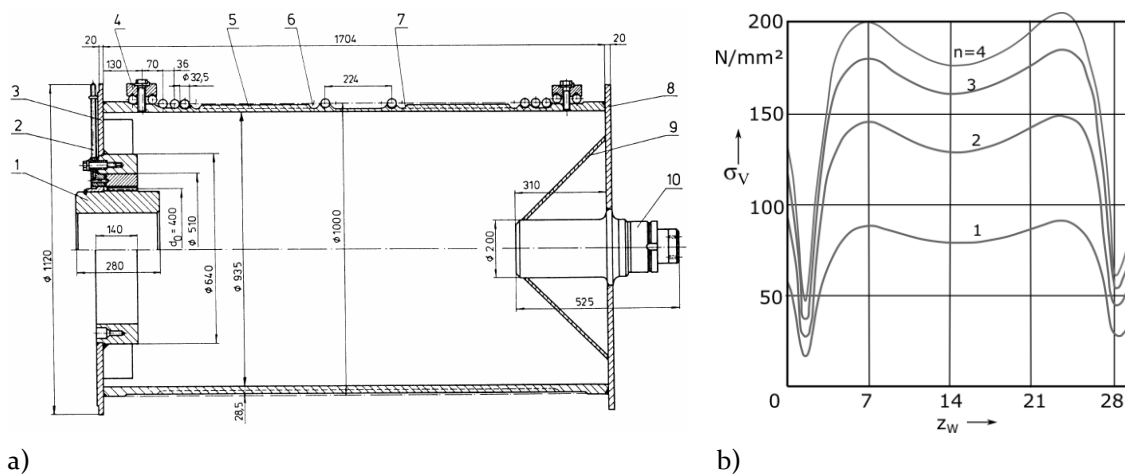

Figure 2: Conventional rope drum; a) exemplary design, b) stress in drum shell along drum axis [9]

Despite the above-mentioned advantages, FFF is not yet used to any significant extent to produce conventional machine elements. This is primarily due to the lack of knowledge about the mechanical stability of FFF machine elements. The investigations described below are therefore devoted to the stability of FFF machine elements using the rope drum as an example, as it is a widespread machine element in material handling.

Rope drums generally consist of a drum body (5), on which the rope is wound, two flanges (3, 8), which prevent the rope from slipping off, and a hub (1, 10), which connects the drum to the drive shaft (**Figure 2**a). Rope drums come in single- or multi-layer spooling designs with helical or functional groove systems; the latter optimized to prolong rope service life with multi-layer spooling. Wire ropes are still standard in industrial hoists but first crane systems with specialised fibre ropes exist as well [10]. The nominal drum diameter, with which the rope is wound around the drum, depends on the rope diameter and ranges from 10 (lower limit for cranes) to 110 times (upper limit for mining hoists) the rope diameter, depending on the application [9].

The variety of different rope diameters, diameter distributions, and rope lengths to be stored on the drum results in a wide range of variants of rope drums. Due to the rope

tension force, which varies during operation because of e. g. changing loads, the drum shell is subjected to bending, torsion, and compression. Due to its magnitude, only the latter is significant in regard to the drum body's structural stability. The stress σ_V in the drum body varies in the direction of its length z_W, with the number of spooled layers n, and between parallel and pitch areas of a functional groove system, resulting in a complex load case (**Figure 2**b) [11]. Previous studies have already compared the stability of FFF drum bodies with different infill structures [12]. Drum bodies with a mass of 190 g reached breaking forces of up to 3.2 kN, resulting in a specific breaking force

$$F_b^* = \frac{F_b}{m_T} \tag{2}$$

of 17.5 kN/kg. The best results were achieved both with a gyroid-TPMS and a straight spokes infill structure. To determine whether a combination of both infill structures leads to a further increase in stability, the following investigations are dedicated to the experimental analysis of a drum body with a novel hybrid infill structure that consists of part gyroid-TPMS and part straight spokes.

2. Methods

A drum body with said hybrid infill structure was designed to serve as test specimen for experiments aimed at the stability of FFF machine elements. Subsequently, the breaking force was determined in custom tensile tests.

2.1. Test specimen design

Figure 3 shows the design of the drum body. It consists of the shell surface (green) and the space provided for the infill structure (orange). It is a drum body suitable for winding wire ropes with 8 mm diameter. The diameter ratio in the first layer is 18 and typical for drum winches in cranes. The drum shell contains a functional groove system according to [13], which runs in parallel and pitch areas. **Table 1** shows the drum body's dimensions. Previous iterations in [12] used feather key connections, which led to unfavourable pressure peaks at higher loads. Therefore, the hub possesses a HTD 8M toothing as an improved shaft-hub joint. The rope end connection is friction-locked, for which the rope is clamped between the drum body and an additional clamping element (**Figure 3**d, blue). Since the infill structure's stability was the subject of the experiments, the test specimen consists exclusively of the drum body without the flanges. These would stabilise the rope drum in axial direction, which was – unlike in practise – not desired for the experiments. The drum body with its groove system, hub, and part of the rope end connection was manufactured in one production step. This demonstrates how the freedom of design that comes with AM could benefit conventional machine elements.
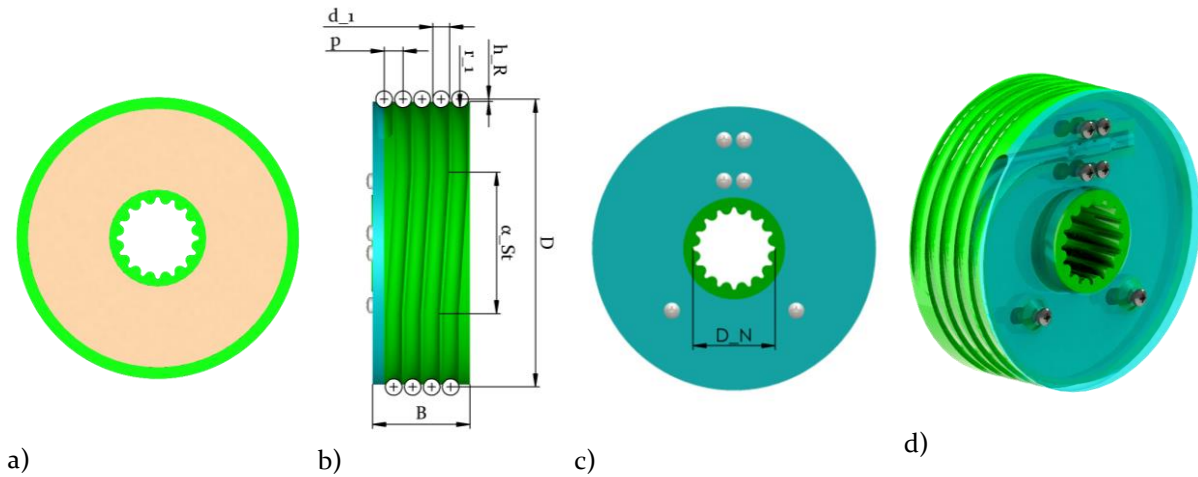
Figure 3: Illustration of test specimen; a) bottom view, b) side view, c) top view, d) isometric view with transparent clamp element

Table 1: Rope drum measurements

Measure-ment	D in mm	h_R in mm	r_1 in mm	B in mm	p in mm	n_W in mm	D_N in mm	z_N	α_{St}	d_1 in mm
Value	144.4	3.0	4.2	42.96	9.5	4	41.10	16	60°	8

The drum body's infill structure consists of two substructures that have proven to be particular advantageous in previous investigations: classical straight spokes and a cylindrical gyroid TPMS structure as shell lattice. The combination of both allows to manipulate the infill distribution μ in addition to the infill density ρ. μ is the volumetric ratio

$$\mu = \frac{V_{Sp}}{V_{TPMS}}$$ (3)

between spokes and gyroid-TPMS substructure. The design of the gyroid-TPMS as well as the merging of both substructures was performed in nTopology's nTop software, which is specifically designed to create AM components. The spokes' and gyroid infill's thickness are both 1.2 mm. All test specimens shown are made of the colourless PLA "BASF Ultrafuse" to prevent possible interference from colour particles [14]. The test specimens were printed on a "Ultimaker 2+" FFF 3D printer from manufacturer Cura. They were printed in such a way that the open side surface laid on the print bed and the print layers run perpendicular to the drum axis. **Table 2** contains the used printing parameters.

Table 2: Print parameters

Quantity	Value
Print direction	along drum axis
Build plate adhesion type	none (brim for ρ=0.3)
Layer height	0.15 mm
Primary layer height	0.15 mm
Infill line width	0.4 mm
Inner wall(s) line width	0.4
Extra skin wall count	0
Z-Seam alignment	random
Wall line count	10
Outer wall speed	40 mm/s
Top/Bottom speed	30 mm/s
Infill speed	60 mm/s
Initial layer speed	15 mm/s
Print speed	60 mm/s
Infill pattern	lines
Infill density	100%
Printing temperature	215°C

2.2. Experimental setup

Figure 4 shows the chosen experimental setup. The drum body sits on a geared shaft between two bearing brackets. The geared shaft connects to the bearing brackets through two FFF sleeves that possess the HTD 8M toothing. This made for a cost-efficient shaft-hub connection for the experimental setup. One of the two bearings was fixed by a cross pin connection to prevent rotation.

A typical hoisting rope for cranes (rotation-free wire rope 8 mm 16x7-IWRC) was spooled to half the width of the drum and transmitted the rope tension force. Further spooling was rejected for the following reasons: Multi-layer spooling would lead to spooling failures disturbances without the recommended rope tension force (1 kN, 2 % of the minimum breaking load of the wire rope), as each test run began with a relaxed rope. A completely spooled first layer led to the test specimen's premature breakage at the side where the wire rope runs off the drum. This is caused by the missing axial stabilisation from the drum flanges. Because the stability of the drum body by itself was the subject of the experiments, it was decided to not install drum flanges and the drum was spooled up to its centre. The test happened quasi-statically by slowly increasing the rope tension force. Failure by breaking of the test specimen marked the end of a test run.
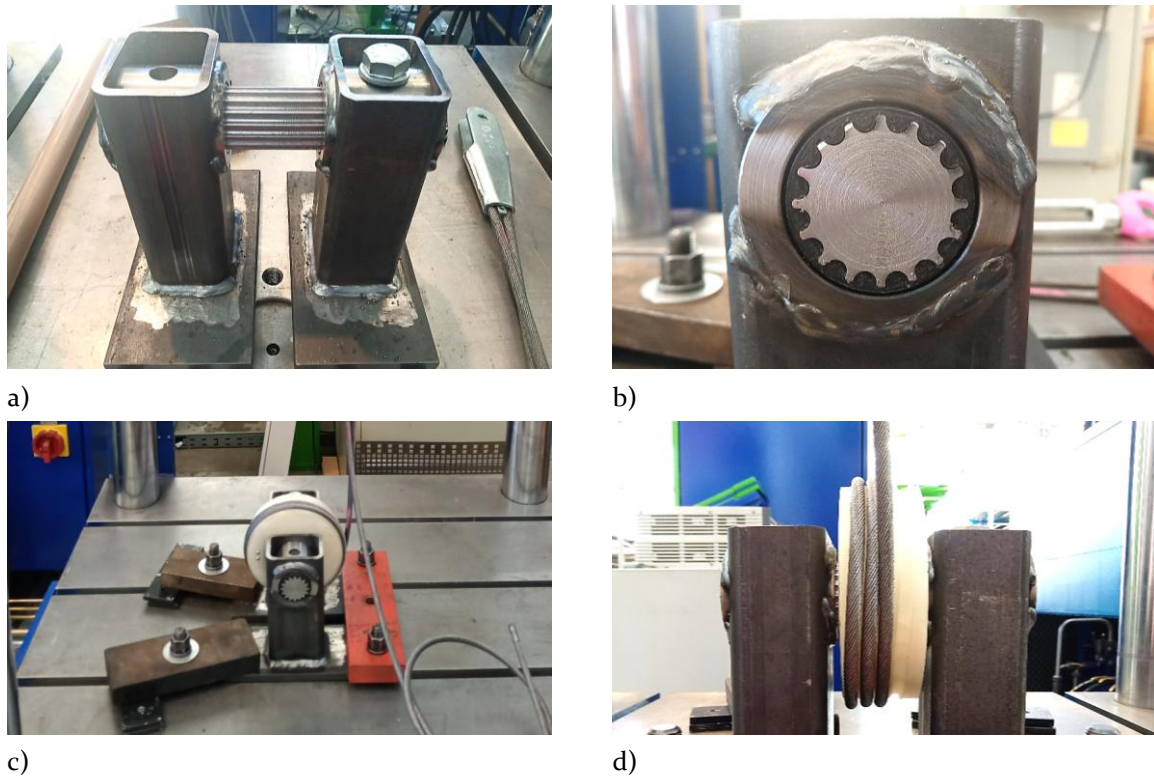
Figure 4: Experimental setup; a) Bearing block with splined shaft, b) Shaft-hub connection in bearing block with toothed FFF sleeve (black), c) overview, d) spooled rope on drum body

Table 3: Experimental design

Run	Specimen ID	n_{Sp}	l_C in mm	n_C	V_{Sp} in cm³	V_{TPMS} in cm³	V_{res} in cm³
1	0107_a	6	42	15	18,9	26,1	43,7
2	0107_b	6	42	15	18,9	26,1	43,7
3	0110	7	50	15	22,1	22,4	43,5
4	0113_a	8	57	11	25,2	19,6	43,6
5	0113_b	8	57	11	25,2	19,6	43,6
6	0207	12	20	28	37,2	52,2	84,7
7	0210_a	14	25	26	43,2	43,5	82,4
8	0210_b	14	25	26	43,2	43,5	82,4
9	0210_c	14	25	26	43,2	43,5	82,4
10	0213	16	29	23	49,2	38,2	82,7
11	0307_a	18	14	42	54,7	76,3	121,2
12	0307_b	18	14	42	54,7	76,3	121,2
13	0309	21	15	29	63,2	63,8	117,2
14	0313_a	25	18	30	74,4	57,3	121,3
15	0313_b	25	18	30	74,4	57,3	121,3
16	0313_c	25	18	30	74,4	57,3	121,3

2.3. Experimental design and evaluation

The experimental design serves the purpose of determining the influences of the infill density ρ and distribution μ on the breaking force F_b. For this purpose, a screening design contains 16 test runs (**Table 3**). ρ takes values of 0.1, 0.2 and 0.3, while μ varies between 0.7, 1.0 and 1.3. To achieve this, the number of spokes n_{Sp} as well as the cell size l_C and number n_C of the TPMS were adjusted accordingly (**Figure 5**). In addition, **Table 3** lists the resulting volumes V_{Sp} and V_{TPMS} of both substructures as well as the total volume V_{res} of the hybrid infill structure. V_{res} is smaller than the sum of V_{Sp} and V_{TPMS}, as both substructures overlap, but the overlap does not increase the total volume.
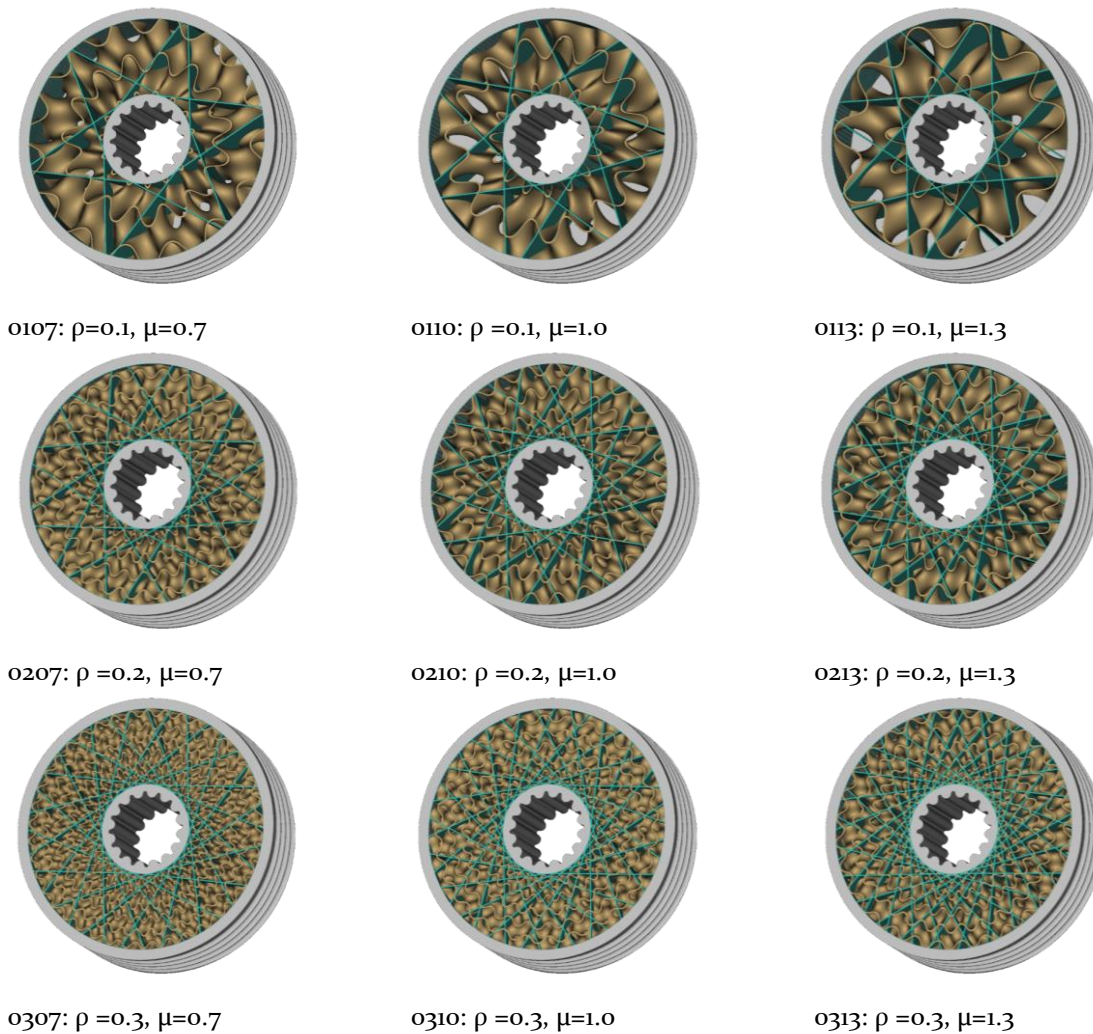

0107: ρ =0.1, μ=0.7	0110: ρ =0.1, μ=1.0	0113: ρ =0.1, μ=1.3
0207: ρ =0.2, μ=0.7	0210: ρ =0.2, μ=1.0	0213: ρ =0.2, μ=1.3
0307: ρ =0.3, μ=0.7	0310: ρ =0.3, μ=1.0	0313: ρ =0.3, μ=1.3

Figure 5: Novel hybrid infill structure, variation of ρ and μ

3. Results and Discussion

The results of the test series are presented and discussed below.

3.1. Mass and print time

Table 4 contains the test specimens' mass m_T and print time t_p, grouped by infill density ρ. m_T ranges between 215.0 and 337.0 g, while t_p was 26.3 to 46.6 hours. As expected, m_T increases with increasing ρ. The drum bodies' solid walls amount to 164.0 g. This equates to a fraction of 75%, 61% and 49% of the test specimens' mass for ρ=0.1, 0.2, and 0,3. The print time of the solid walls alone is 16.2 hours and represents 61, 45 and 35 % of the test specimens' print time for ρ=0.1, 0.2, and 0,3. The higher relative mass share compared to the relative print time originates from the fact that the solid walls accumulate a lower number of empty movements for the print head than when printing porous infill structures.

Table 4: Test specimen mass and print time, sorted by infill density

	Infill density ρ							
	0.0 (only walls)		0.1		0.2		0.3	
	m_T in g	t_p in hh:mm	m_T in g	t_p in hh:mm	m_T in g	t_p in hh:mm	m_T in g	t_p in hh:mm
Mean	164.0	16:13	217.4	26:43	269.2	36:26	331.7	45:35
Min.	-	-	215.0	26:19	266.0	36:21	324.0	43:55
Max.	-	-	219.0	27:04	277.0	36:46	337.0	46:37
Std.-Error	-	-	0.7	0:10	2.0	0:05	2.1	0:24

3.2. Test execution and damage pattern

Figure 6 shows the rope tension force over the testing machine's stroke z, grouped by ρ. A similar behaviour is visible for all runs. A linear increase is followed by a peak resembling the breaking force and a sudden drop in rope tension force when the drum body breaks. In most cases, the global peak is preceded by a sudden increase. A positive correlation is visible between F_b and ρ. **Figure 7** shows the similar grouping for the infill distribution μ, which exhibits no F_b and μ.
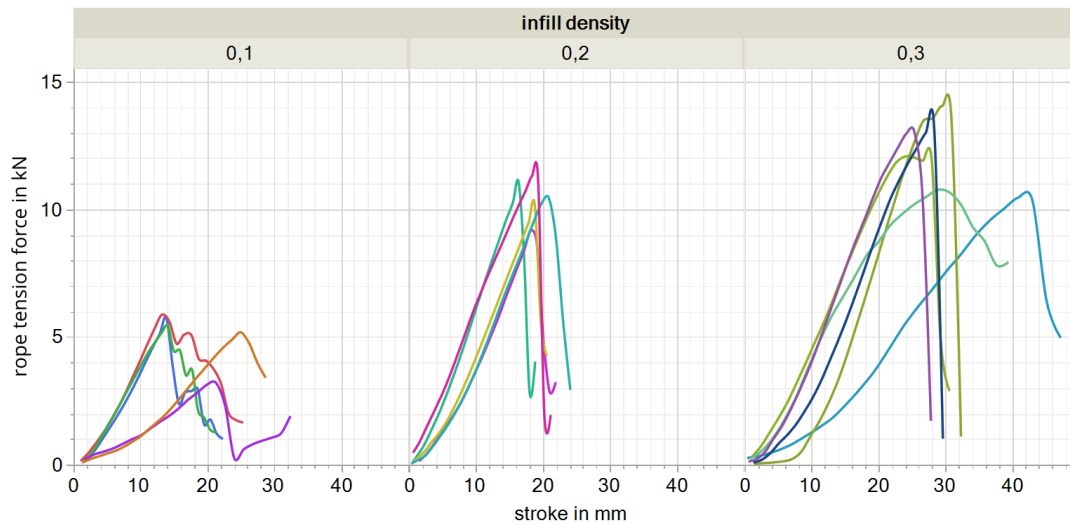
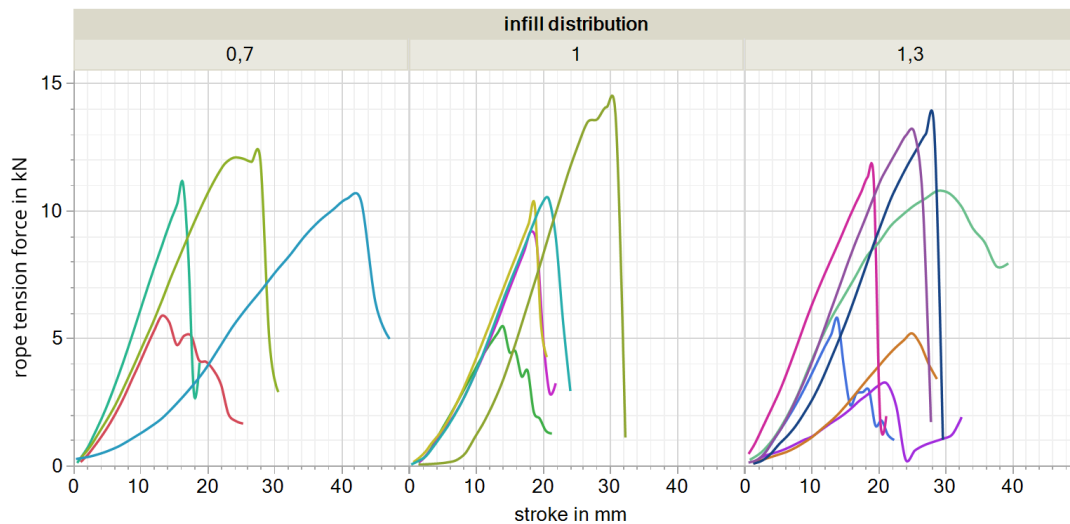**Figure 6:** Force over stroke, grouped by infill density ρ

Figure 7: Force over stroke, grouped by infill distribution μ

The general damage pattern is similar for all runs. A brittle fracture occurs at the groove where the rope leaves the drum, which results from the drum body delaminating along the print layers. This represents a weak point of FFF components, which must be taken into account in the design of FFF machine elements; either through reorienting the component on the print bed, through adjusting the infill structure, or through stabilising the component externally. For the drum body, the latter could be accomplished by adding two flanges. Visible damage can be seen to varying degrees on the infill of the test specimens. For ρ=0.1, highly visible fractures occur in the infill structure, whereas for ρ=0.3 no damage is visible within it (**Figure 8**). In both cases, the drum body splits at the leaving rope (**Figure 9**). Depending on the breaking force, a different depth of retraction of the wire rope into the drum body can be observed. The damage patterns for ρ=0.3 suggest that the stability of the hybrid infill structure has already exceeded that of the drum shell. This must be considered in the following examination of the breaking force and deformation.
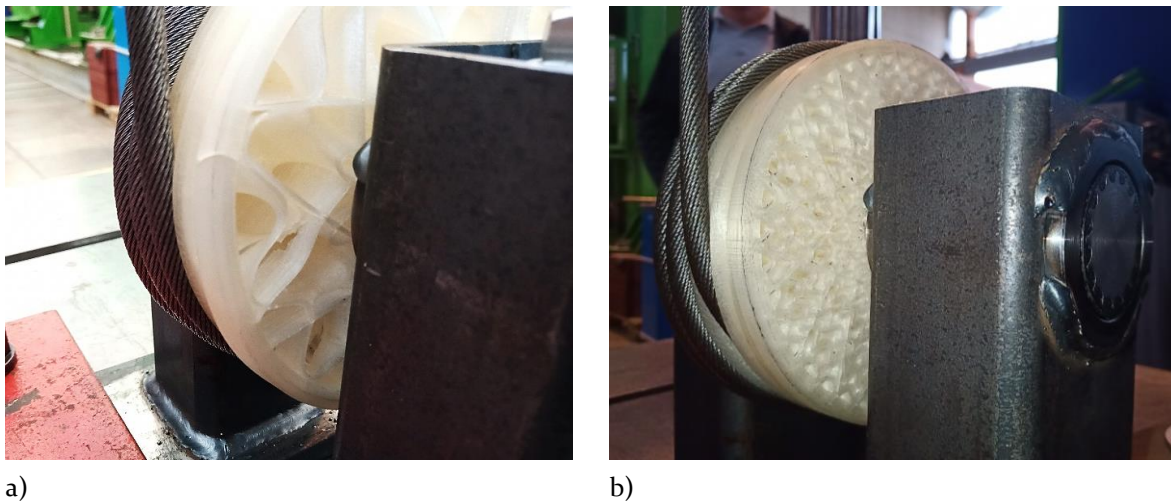
a)   b)

Figure 8: Drum body at end of testing, view at infill structure; a) ρ=0.1, b) ρ=0.3

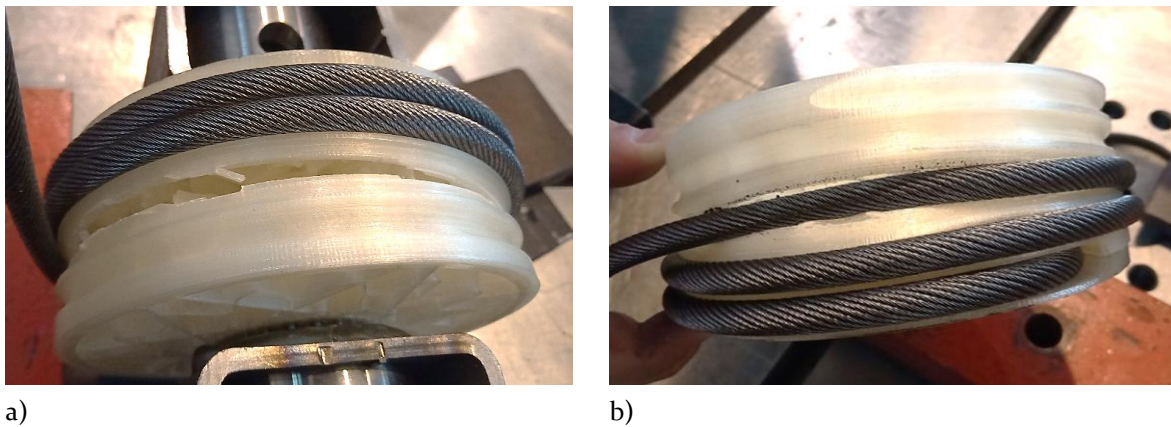a)   b)

Figure 9: Drum body at end of testing, view at groove; a) ρ=0.1, b) ρ=0.3

3.3. Breaking force

Figure 10 shows the achieved breaking forces sorted by test specimen. F_b and F^*_b are shown next to each other. The values for ρ and μ can be read from the specimen ID (**Figure 5**). **Table 5** contains the mean F_b and F^*_b, which range from 3.3 to 14.7 kN and 15.1 to 45.4 kN/kg. From ρ=0.1 to 0.2, F_b increases by an average of 5.2 kN (+102%), resulting in an increase in F^*_b of 15.9 kN/kg (+64%). From ρ=0.2 to 0.3, F_b increases only by 1.6 kN (+14%). This results in a reduction of F^*_b by 3.0 kN/kg (-7%). It can be stated that F_b and F^*_b generally increase with increasing ρ, though further investigations are necessary to interpret the results for ρ=0.3. The damage pattern described in section 3.2 suggests that the infill structure's stability exceeds the drum shell's and that a redesigned drum body will show better results for ρ=0.3. It cannot be ruled out yet that a negative correlation between F_b or F^*_b and ρ will develop from ρ=0.3 upwards. The infill distribution μ shows the following trends for F_b and F^*_b: Initially F_b and F^*_b increase from μ=0.7 to 1.0 by 1.1 kN (+12%) and 2.5 kN/kg (+13%). From μ=1.0 to 1.3 there is a decrease of 0.8 kN (-8%) and 5.6 kN/kg (-15%). This means that out of the tested μ=1.0 is the optimal setting, although μ affects the F_b and F^*_b significantly lower than ρ.
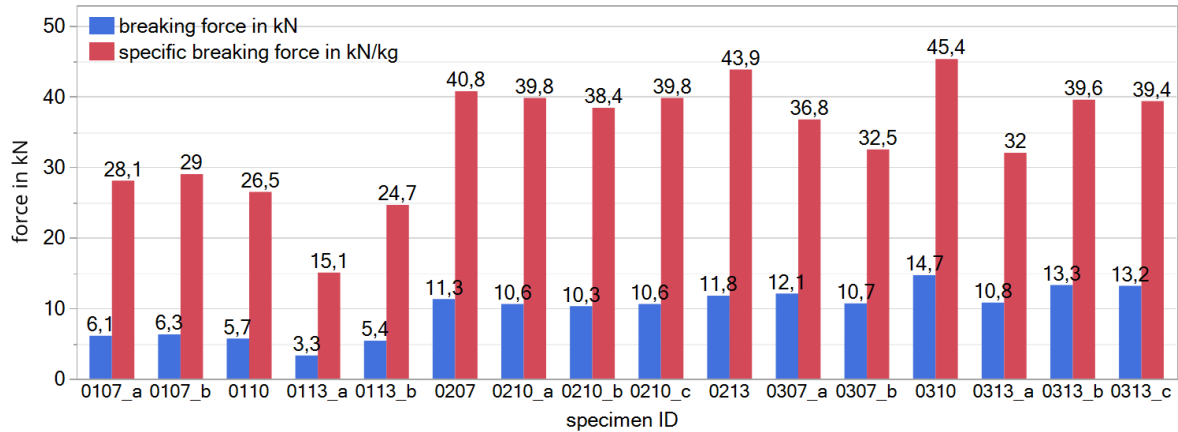
Figure 10: Total and specific breaking force sorted by specimen ID

Table 5: Mean breaking forces sorted by infill density and distribution

	Infill density			Infill distribution		
	0.1	0.2	0.3	0.7	1.0	1.3
F_b in kN	5.4	10.9	12.5	9.3	10.4	9.6
F_b^* in kN/kg	24.7	40.6	37.6	33.5	38.0	32.4

In comparison with the previous investigations from [12], it is shown that the combination of a gyroid-TPMS and a straight spokes infill leads to a significant improvement in stability. The specific breaking force F_b^* exceeds the previous results (maximum 17.5 kN/kg) for every tested combination of ρ and μ and reaches a maximum increase of 159% (45.4 kN/kg).

3.4. Stiffness

Due to the complex deformation of the drum body, uniaxial strain cannot be determined as a measure of the test specimens' stiffness. The test specimens' deformation was therefore quantified by indirect measurement of the test machine's stroke z. **Figure 11** shows the stroke that occurs at maximum rope tension force, subtracted by the wire rope's elongation. **Table 6** lists the mean deformation Δz for each level of ρ and μ.
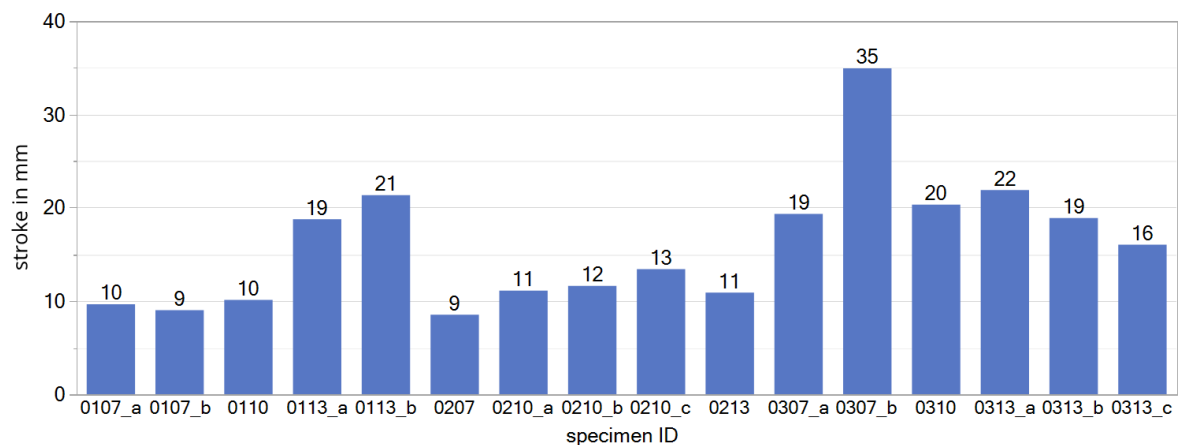

Figure 11: Stroke at test specimens' failure, sorted by specimen ID

Table 6: Stroke over infill density and distribution

	infill density			Infill distribution		
	0.1	0.2	0.3	0.7	1.0	1.3
Δz	14	11	22	16	13	18

A stiffening occurs from ρ=0.1 to ρ=0.2 (-3 mm, -21%), while from ρ=0.2 to 0.3 elasticity increases strongly (+11 mm, +100%). Considering the damage patterns from section 3.2, it can be stated that an increase of ρ is accompanied by a stiffening of the infill structure, provided that the test specimen fractures predominantly inside the infill structure. Otherwise, a more ductile damage pattern was observed for ρ=0.3. With regard to the infill distribution μ, a balanced distribution of μ=1.0 yields the highest stiffness (Δz=13 mm). Deviations in both directions lead to a stronger deformation of 16 mm (+23%) for μ=0.7 and 18 mm (+38%) for μ=1.3.

4. Conclusion

Static tensile tests determined the breaking force and deformation of FFF rope drums. The test specimens possess a novel, hybrid infill structure consisting of a gyroid-TPMS structure and a conventional arrangement of straight spokes. The infill density ρ varied between 0.1, 0.2 and 0.3. The infill distribution μ, which describes the volumetric ratio of spokes to gyroid TPMS structure, varied between 0.7, 1.0 and 1.3.

The test specimens' damage pattern shows damage to the infill structure for ρ=0.1, whereas only superficial damage at the groove is visible ρ=0.3. Common to all tests is a delamination of the print layers along the drum axis, which is equal to the print direction.

The tests show breaking forces of up to 14.7 kN, which results in a specific breaking force of 45.4 kN/kg. This means that the maximum specific breaking forces achieved in previous tests with simple infill structures could be increased by up to 159%. Furthermore, a positive correlation between infill density and breaking force was observed, although a plateau formed at ρ=0.3. Further investigations with a redesigned drum body must show whether this is due to the failure of the drum shell or the infill structure. The infill distribution has small influence on the breaking force but a balanced distribution of μ=1.0 achieves the best results.

The test specimens' stiffness correlates positively with infill density between ρ=0.1 and ρ=0.2. For ρ=0.3, a strong increase in deformation is observed, which may originate from the drum shell's superficial failure. Again, further tests with a redesigned drum body are advised to confirm this conclusion. The infill distribution also affected the test specimens' stiffness. A balanced distribution of μ=1.0 yields highest stiffness.

The presented investigations demonstrate the great potential of FFF machine elements such as rope drums. The recorded specific breaking forces draw a realistic perspective for the use in future products like drum hoists. Through a novel, hybrid infill structure, the stability of the tested drum bodies was increased compared to previous investigations. This goes hand in hand with other advantages of AM like a lean

manufacturing process that allows the production of drum bodies with functional groove systems, a grooved shaft hub and the rope end connection in one step.

References

[1]   Choudhari CM, Patil VD (2016) Product Development and its Comparative Analysis by SLA, SLS and FDM Rapid Prototyping Processes. Mater. Res. Express 149:12009. doi:10.1088/1757-899X/149/1/012009

[2]   Deutsches Institut für Normung e. V. (1977) Krane; Rillenprofile für Seiltrommeln (DIN 15061-2). Beuth Verlag GmbH, Berlin, DE

[3]   Hofmann R, Matthes C, Schmidt T (2020) Capabilities of Additively Manufactured Rope Drums. innoTRAC 1:26–36. doi:10.14464/innotrac.v1i0.461

[4]   Jeremic S, Milovanovic J, Mojicevic M, Skaro-Bogojevic S, Nikodinovic-Runic J (2020) Understanding bioplastic materials - current state and trends. J Serb Chem Soc 85(12):1507–1538. doi:10.2298/JSC200720051J

[5]   Jin Y, Kong H, Zhou X, Li G, Du J (2020) Design and Characterization of Sheet-Based Gyroid Porous Structures with Bioinspired Functional Gradients. MATERIALS 13(17):3844. doi:10.3390/ma13173844

[6]   Kladovasilakis N, Tsongas K, Tzetzis D (2020) Finite Element Analysis of Orthopedic Hip Implant with Functionally Graded Bioinspired Lattice Structures. Biomimetics (Basel) 5(3). doi:10.3390/biomimetics5030044

[7]   Morão A, de Bie F (2019) Life Cycle Impact Assessment of Polylactic Acid (PLA) Produced from Sugarcane in Thailand. J Polym Environ 27(11):2523–2539. doi:10.1007/s10924-019-01525-9

[8]   Mupende I (2001) Beanspruchungs- und Verformungsverhalten des Systems Trommelmantel - Bordscheiben bei mehrlagig bewickelten Seiltrommeln unter elastischem und teilplastischem Werkstoffverhalten. Zugl.: Clausthal, Techn. Univ., Diss., 2001. Cuvillier, Göttingen

[9]   Mupende I (2020) Faserseile für Kranapplikationen: Herausforderungen für die Entwicklung und den Einsatz auf dem Liebherr Turmdrehkram. in: Katterfeld A, Richter K, Krause F, Pfeiffer D (Hrsg) 28. Internationale Kranfachtagung. KRAN 4.0: Potenziale der Digitalisierung, Magdeburg, DE, S 5–18

[10]   Scheffler M (1994) Grundlagen der Fördertechnik - Elemente und Triebwerke. Fördertechnik und Baumaschinen. Vieweg+Teubner Verlag, Wiesbaden, s.l.

[11]   Schnering HG von, Nesper R (1991) Nodal surfaces of Fourier series: Fundamental invariants of structured matter. Z. Physik B - Condensed Matter 83(3):407–412. doi:10.1007/BF01313411

[12]   Shi X, Liao W, Liu T, Zhang C, Li D, Jiang W, Wang C, Ren F (2021) Design optimization of multimorphology surface-based lattice structures with density gradients. Int J Adv Manuf Technol 139(6):(1009051O). doi:10.1007/s00170-021-07175-3

[13]   Waller JM, Saulsberry RL, Parker BH, Hodges KL, Burke ER, Taminger KM (2015) Summary of NDE of additive manufacturing efforts in NASA 41ST ANNUAL REVIEW OF PROGRESS IN QUANTITATIVE NONDESTRUCTIVE EVALUATION: Volume 34. AIP Publishing LLC, S 51–62

[14]   Wittbrodt B, Pearce JM (2015) The effects of PLA color on material properties of 3-D printed components. ADDITIVE MANUFACTURING 8(01):110–116. doi:10.1016/j.addma.2015.09.006